I&EC research
Industrial & Engineering Chemistry Research



pubs.acs.org/IECR
Article

# Impact of Permeability of Triply Periodic Minimal Surface-Based Substrates on Multiwalled Carbon Nanotube Growth

*Published as part of Industrial & Engineering Chemistry Research special issue "Smart Reactors - Towards Adaptive, Resilient, and Autonomous Process Systems".*

Fabian Riebesehl,* Serhan Acikgöz, Timo Merbach, Christiane Roller, Dominique Lumpp, Dirk Herzog, Jakob Albert, Ingomar Kelbassa, Michael Schlüter, and Bodo Fiedler

Cite This: *Ind. Eng. Chem. Res.* 2026, 65, 16002−16013

Read Online

ACCESS | Metrics & More | Article Recommendations | Supporting Information

**ABSTRACT:** Due to their excellent thermal and electrical properties combined with pronounced porosity, carbon nanotube forests are promising as catalyst support materials for smart reactors. To maximize catalytic turnover, it is essential to increase the available surface while maintaining precise control over reactant flow and heat distribution. In this work, multiwalled carbon nanotubes are grown on three-dimensional substrates based on triply periodic minimal surfaces, which offer superior mechanical properties alongside controlled flow dynamics and enhanced heat transfer rates. The substrates are fabricated via laser powder bed fusion and subsequently coated using injection chemical vapor deposition. To evaluate the design limitations of the three-dimensional substrates for CNT growth, the impact of a decreasing permeability on the coating's morphology is investigated. As the permeability decreases with the unit cell size of the triply periodic minimal surfaces and the introduction of an external wall, the characteristic CNT forest structure gradually transforms. Provided that permeability and precursor accessibility to the internal surfaces remain sufficiently high, the morphology and composition of CNT forests closely resemble those grown on flat substrates. Introducing the wall leads to a transition from vertically aligned CNT forests to horizontally oriented CNT networks due to enhanced laminar-like flow characteristics. While less dense, it offers an increased CNT quality. Below a critical minimal permeability, carbon nanostructures with numerous defects form. The successful coating and control of its morphology enable the utilization of the CNT for further smart tailoring of the reactor.

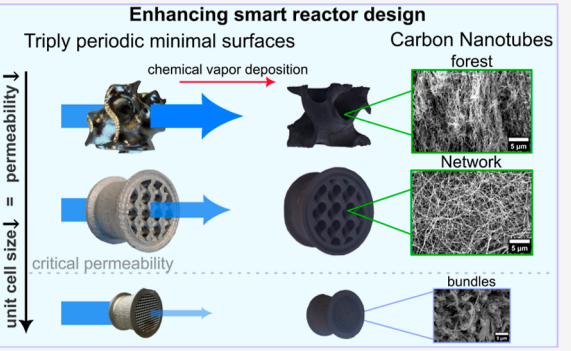


## INTRODUCTION

Carbon nanotubes (CNTs) have gathered substantial interest for industrial applications due to their exceptional thermal, electrical, and mechanical properties.[1,2] Numerous advanced strategies for the smart utilization of CNTs include their application as thermal interface materials, as energy storage systems, and the exploitation of their switchable wetting behavior.[3−5] Since the development of the large-scale catalytic chemical vapor deposition (CVD) technique, intense research efforts have focused on optimizing their growth processes and material characteristics.[6−8] For instance, steady-state growth of CNTs on substrates is enabled by injection CVD, which continuously feeds catalyst precursors in addition to a carbon source into the process.[9] During this process, the catalyst precursors, often metallocenes like ferrocene, are reduced to the metal atoms.[9,10] These collide and coalesce to form larger catalyst particles.[11] The constant injection enables a continuous formation of new CNT growth sides on the substrate. The catalyst size and distribution determine the homogeneity and quality of CNT coating as one catalyst particle induces the growth of one single CNT.[10,11] The simplicity and scalability of CVD offer key advantages, allowing the tailored synthesis of various CNT coatings through precise control of process parameters including the temperature, the feeding rate, or the choice of precursor and substrate.[9,10] These critically influence CNT morphology, alignment, and defect density, which in turn impact their performance.[9] During CVD growth, spatial confinement by neighboring nanotubes promotes their perpendicular alignment relative to the substrate, resulting in vertically aligned CNT (VACNT) forests.[12,13] These forests form complex porous structures, where intertube spacings commonly range between 10 and 100 nm, depending on their packing density and waviness.[14] Their high surface area and

Received: March 12, 2026
Revised: July 3, 2026
Accepted: July 5, 2026
Published: July 22, 2026

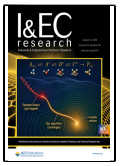





https://doi.org/10.1021/acs.iecr.6c01128
*Ind. Eng. Chem. Res.* 2026, 65, 16002−16013

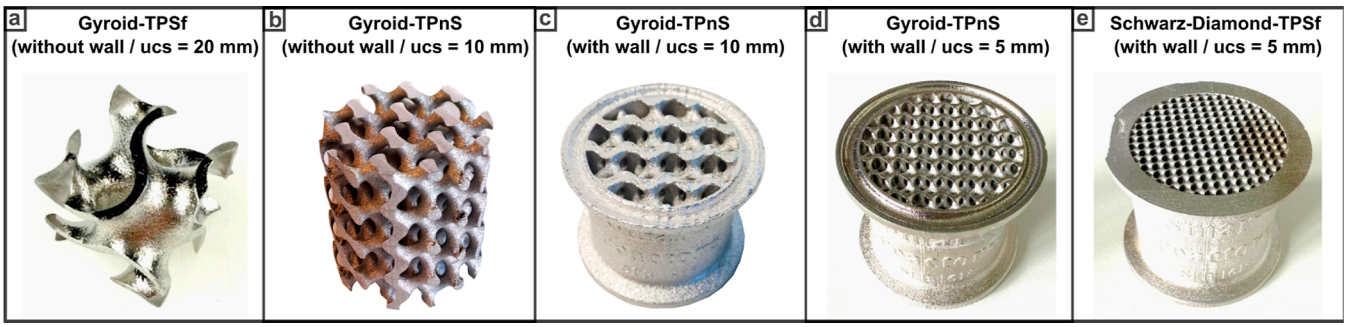


**Figure 1.** TPMS structures used in this study after electrochemical polishing: (a) Gyroid-TPSf (ucs = 20 mm, without wall), (b) Gyroid-TPnS (ucs = 10 mm, without wall), (c) Gyroid-TPnS (ucs = 10 mm, with wall), (d) Gyroid-TPnS (ucs = 5 mm, with wall), and (e) Schwarz-Diamond-TPSf (ucs = 5 mm, with wall). All TPMS structures exhibit a target porosity of $\epsilon$ = 70%.

accessible active sites make VACNT forests promising candidates for catalyst supports.[15−18] However, much of this potential remains untapped when CNTs are grown on conventional two-dimensional substrates of alumina, silicon, or quartz glass.[10] Silicon and quartz glass enable rapid growth of well-aligned CNT forests thanks to favorable surface properties, including low surface energy, smoothness, and suitable diffusivity, but their brittleness limits their practical utility.[1,19] In contrast, metallic substrates generally produce CNT forests with lower alignment quality[19] but offer superior electrical conductivity and improved mechanical processability.[1] CNT growth on various fibrous materials has been extensively studied.[20−22] By comparison, investigations into porous three-dimensional substrates remain relatively scarce. Although CNTs have been successfully grown on porous templates such as anodic aluminum oxide or channeled ceramic monoliths, these substrates are limited by their internal surface geometry.[23,24] Specifically, their low curvature and straight-channel designs restrict the maximization of available surface area. Other studies have explored more complex porous materials like carbon aerogels[25] or mesoporous molecular sieves,[26] which, however, show limited structural control.

A class of three-dimensional structures that combine high structural complexity with precise design control is triply periodic minimal surfaces (TPMSs). Defined by their three-dimensional periodicity and continuous curvature,[27] TPMSs possess high surface-to-volume ratios and specific surface areas, resulting in both pronounced porosity and excellent mechanical stability.[28−30] Their open structure and smooth, edge-free geometries enable an intensive convective flow through the VACNT with enhanced heat and mass transfer, which render them especially advantageous for reactor design applications.[28,31] TPMS permeability depends on factors such as its unit cell size (ucs), porosity $\epsilon$, and TPMS type as it tends to decrease with smaller unit cell sizes and higher porosities.[32] Consecutively, the specific surface area of TPMS structures increases with decreasing ucs, nearly halving between 20 mm, 10 mm, and 5 mm, respectively.[33] In addition, lowering the ucs significantly decreases convective transport and heat and mass transfer inside the TPMS structure.[33] Among the most widely studied TPMS geometries are the Gyroid and Schwarz-Diamond structures. While the Schwarz-Diamond TPMS demonstrates lower permeability due to its reduced pore dimensions,[34,35] it exhibits a higher specific surface area, as well as convective heat and mass transfer.[33] Additive manufacturing methods, in particular laser powder bed fusion (PBF-LB/M), enable the precise fabrication of complex three-dimensional metallic structures including TPMS-based substrates.[36] This technique selectively melts and fuses metal powder layers with a laser, producing fully dense components.[37] Since mathematically ideal TPMSs are infinitely thin surfaces, practical realizations require a finite wall thickness. Following the nomenclature by Fisher et at.,[38] variants based on the original TPMS definition, such as triply periodic surface structures (TPSf), triply periodic endoskeletons (TPnS), and triply periodic exoskeletons (TPxS), can be fabricated. TPSf structures directly replicate the TPMS , whereas TPnS and TPxS are derived from the interior volume enclosed by the surface.[38] The PBF-LB/M approach facilitates the development of TPMS-based substrates tailored for CNT growth by combining the optimized flow and thermal properties of TPMSs with the high porosity as well as the superior thermal and electrical characteristics of CNT coatings. While TPMS structures are already recognized as promising designs for SMART reactors[33] and catalytic processes on additively manufactured supports have been established,[39−41] the application of CNT coatings to these supports is expected to further enhance their catalytic performance. These tailored smart reactors could serve as direct alternatives to conventional fixed-bed reactors, which dominate industrial processes.[42] While fixed-bed reactors offer high catalytic surface areas, their flow dynamics are complex and less controllable compared to TPMSs.[43] Furthermore, the micro structuring of the CNT coating on TPMS substrates enables additional tuning and enhancement of catalytic performance.[44,45] In this study, porous stainless-steel substrates with different TPMS geometries are manufactured by PBF-LB/M. Their surfaces are subsequently coated with multiwalled carbon nanotubes (MWCNTs) using the injection CVD method. We investigate how the manufacturing process and the unit cell size of the TPMS substrates influence CNT growth on the inner surfaces. Therefore, the morphology and structure of CNT carpets on various substrates are characterized. Based on these findings, the suitability of MWCNT-coated TPMS structures as catalyst supports in smart reactors is assessed.

## EXPERIMENTAL SECTION

### Selection, Manufacturing, and Surface Treatment of TPMS Structures

In this study, five distinct TPMS structures and a plate with dimensions of 10 × 10 × 1 mm$^3$ are examined to investigate the influence of structural complexity and permeability on the growth of MWCNTs. TPMS geometries are mathematically defined by the





https://doi.org/10.1021/acs.iecr.6c01128
Ind. Eng. Chem. Res. 2026, 65, 16002−16013

smooth, edge-free geometries due to the zero mean curvature at every point. These structures provide high volume-specific surface areas, making them ideal candidates for heterogeneous catalysis.[27,36] The structures were generated using nTopology software (New York, USA), and their designation follows the nomenclature of Fisher et al.[38] The selection comprises of a Gyroid-TPSf, three variants of Gyroid-TPnS, and a Schwarz-Diamond-TPSf, depicted in Figure 1.

Each geometry is characterized by three key design parameters: the unit-cell size (ucs), the target porosity ($\epsilon$), and the sheet thickness ($ts$).[33] To establish a transitional reference between two-dimensional surfaces and complex three-dimensional lattices, the Gyroid-TPSf is designed with a large ucs of 20 mm and a porosity of $\epsilon$ = 70% without an external wall (Figure 1a). In contrast, the intermediate Gyroid-TPnS exhibits a ucs of 10 mm (Figure 1b,c) and the Gyroid-TPnS and Schwarz-Diamond-TPSf structures are designed with a more compact ucs of 5 mm (Figure 1d,e). All TPMS substrates exhibit an identical porosity of $\epsilon$ = 70%. To simulate realistic reactor configurations and control the precursor flow during the CVD process, the structures with a ucs of 5 and 10 mm are integrated into a surrounding cylindrical wall. To determine the impact of the wall on the CNT coating, the Gyroid-TPMS with a ucs of 10 mm is manufactured with and without the wall (Figure 1b,c).[33,46] The physical realization of the substrates is performed via PBF-LB/M using a TruPrint 1000 (Trumpf SE + Co. KG, Ditzingen, Germany). The system is equipped with a 200 W laser and a focal diameter of 55 $\mu$m. The selected material is 316L stainless-steel powder, supplied by SLM Solutions (Lübeck, Germany), which complies with the DIN EN 10088 standard. The powder's spherical particle morphology, with a size distribution between 10 and 45 $\mu$m, is specifically selected to ensure optimal flowability and layer uniformity during the powder bed fusion process. Unlike polymer-based additive manufacturing, PBF-LB/M of stainless steel provides the necessary thermal stability and inherent catalytic properties required for MWCNT growth. A critical limitation of the PBF-LB/M process is the resulting surface roughness, which can lead to inhomogeneous catalyst distribution. To ensure a defined surface morphology for the subsequent synthesis, the substrates undergo an electrochemical polishing procedure. The experimental setup included a laboratory power supply (PSW 80–40.5 GW INSTEK, Veldhoven, Netherlands) and a specialized electrolyte solution, ElpoLux TM Ansatz (Art. No. E1018, ElpoChem AG, Volketswil, Switzerland). Safety thresholds for overvoltage (OVP) and overcurrent (OCP) are established at 40.00 V and 14.85 A, respectively. The process parameters are programmed to a target of 10.54 V and 11.20 A. During the 20 min immersion process, the substrates acted as the anode, with the operating voltage stabilizing between 6 and 7 V at a constant current of 11.20 A. This treatment effectively reduces surface roughness, enabling more uniform initiation of MWCNT forests. All structures were cleaned for 10 min in an ultrasonic acetone bath before being used as a substrate in the CVD synthesis.

## Preparation of CNT Networks on Stainless-Steel Substrates

Multiwalled carbon nanotubes were synthesized on the six different stainless-steel substrates via chemical vapor deposition, following the procedure reported by Kroening et al. .[47] The CVD process was carried out in a horizontal three-zone tube furnace (Carbolite Gero, Neuhausen, Germany) equipped with a quartz glass tube (110 mm × 1100 mm, Glasatelier Saillart BV, Meerhout, Belgium), and an evaporation unit was installed at the entrance of the furnace. A quartz glass plate was positioned between heating zones 2 and 3, onto which the substrate was placed. Particular attention was paid to aligning the internal channels of the TPMS substrates parallel to the gas flow direction within the quartz tube. The three heating zones were set to temperatures of $T_1$ = 200 °C and $T_2$ = $T_3$ = 760 °C, and the evaporation unit was maintained at 200 °C. The heating zones are of equal size and arranged along the flow direction of the reactor. During the heating phase, the reactor was purged with argon (Ar, Westfalen AG, 99.999 vol %, Cottbus, Germany) at a constant flow rate of 400 mL min$^{-1}$. Once the target temperatures were reached, the argon flow was reduced to 200 mL min$^{-1}$, and hydrogen ($H_2$, Westfalen AG, 99.999 vol %, Cottbus, Germany) was introduced at a flow rate of 20 mL min$^{-1}$. After the flow equilibrated, the precursor solution, consisting of 5 wt % ferrocene (Merck KGaA, 98%, Darmstadt, Germany) in toluene (Th. Geyer GmbH & Co. KG, 99.9%, Renningen, Germany), was introduced. The solution was continuously injected into the evaporation unit using a syringe pump (Kisker Biotech GmbH & Co. KG, Steinfurt, Germany) at a rate of 5.5 mL h$^{-1}$ for 3 h. After a total volume of 16.5 mL of precursor solution had been injected, the hydrogen flow was terminated, and the reactor was cooled to room temperature under an increased argon flow of 400 mL min$^{-1}$. Once cooled to room temperature, the coated substrates were removed from the quartz glass tube.

## Morphological and Compositional Characterization of the CNT Coating

For morphological and compositional characterization of the CNT network, the coated substrates were divided at the center, perpendicular to the gas flow direction. Figure 2 shows the preparation of the cross-section of the TPMS substrates for the characterization of the CNT coating with the Gyroid-TPnS substrate (ucs = 10 mm) as an example. All analytical investigations were performed on the inner surface of the substrate, primarily along its struts.

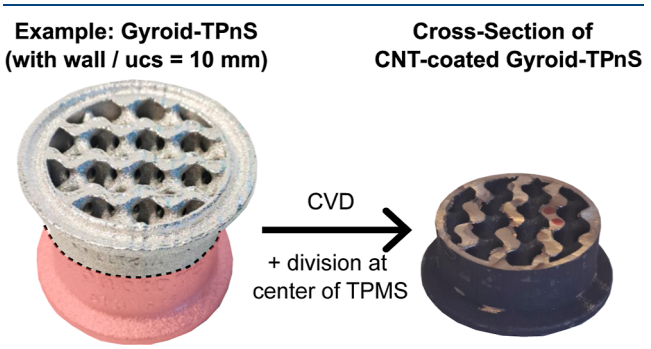


**Figure 2.** Preparation of cross-section of Gyroid-TPnS (ucs = 10 mm, without the wall) via coating and cutting along the center of the substrate.

The morphology of the CNT coating on the different substrates was analyzed by scanning electron microscopy (SEM) using a Zeiss Supra 55 VP (Carl Zeiss AG, Oberkochen, Germany) operated at an acceleration voltage of 2–3 kV. To determine the diameter distribution of the CNTs and carbon nanofilaments, at least 400 individual filaments per substrate were manually measured from SEM images. The measurements were carried out using ImageJ.[48] Compositional analysis was performed by Raman spectroscopy using a TriVista 557 system (Princeton Instruments, Trenton, USA) with an excitation wavelength of 532 nm and a nominal laser power of 30 mW. The measurements were conducted at an effective laser power of 1.6 mW with an acquisition time of 30 s per spectrum. Each measurement was repeated five times at three different sample positions to improve the signal-to-noise ratio. To further investigate the structure of the different carbon species, transmission electron microscopy (TEM) images were acquired by using a FEI Talos F200X transmission electron microscope (Thermo Fisher Scientific, Dreieich, Germany) operated at an acceleration voltage of 120 kV.

# RESULTS AND DISCUSSION

## Morphology of the CNT Coating on Additively Manufactured Substrates

Figure 3 presents SEM images, illustrating the microscopic morphology of CNT coatings on six different stainless-steel substrates.





https://doi.org/10.1021/acs.iecr.6c01128
Ind. Eng. Chem. Res. 2026, 65, 16002–16013

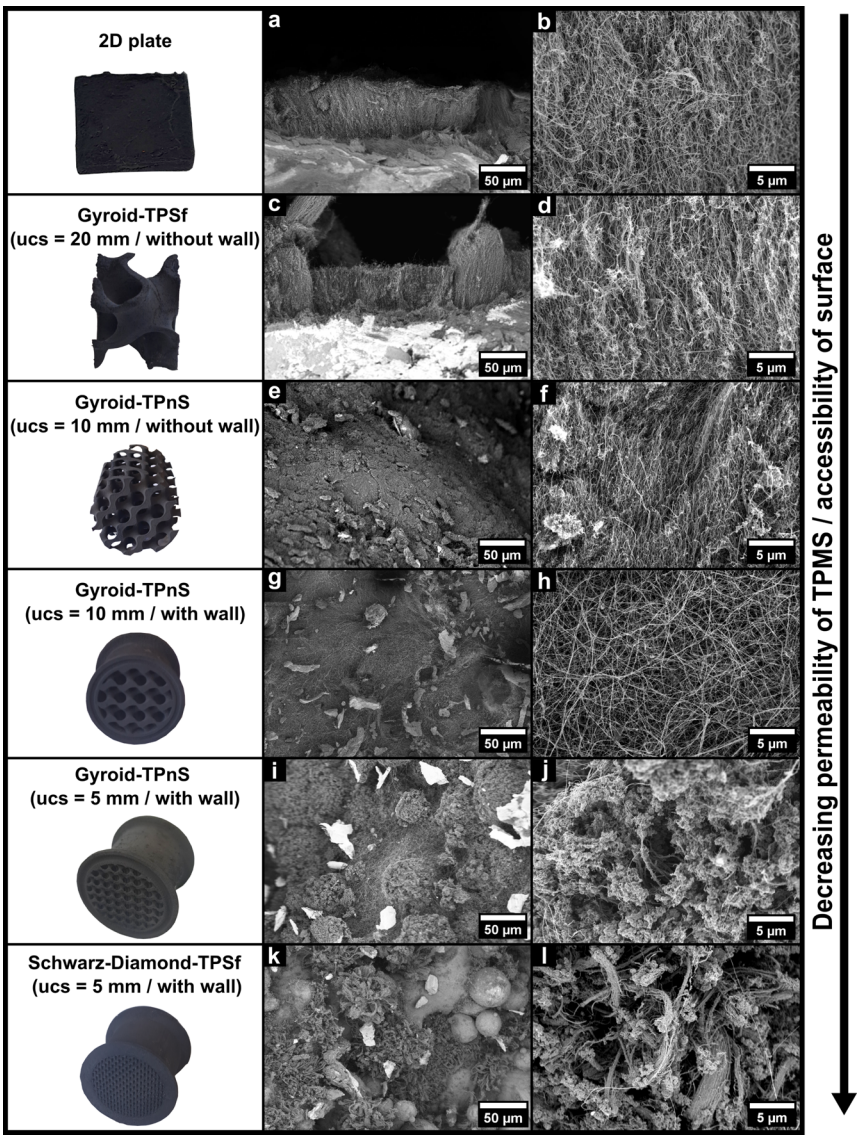


**Figure 3.** Transition of macroscopic shape of the six MWCNT-coated substrates and microscopic structure of the MWCNT coating with decreasing permeability and accessibility of the surface. SEM images show an overview of the microscopic morphology and a close-up of the MWCNT coating on the different substrates.

Initially, a two-dimensional flat plate was produced via PBF-LB/M and coated with MWCNTs to assess the influence of the additive manufacturing process on CNT growth. At low magnification, a dense MWCNT forest is clearly visible (Figure 3a). Due to the spherical morphology of the stainless-steel powder particles used as the precursor, the substrate surface is not perfectly flat but slightly wavy (Figure 3a). This waviness affects the CNT forest growth, resulting in a less homogeneous surface morphology. Although this unevenness is partially reflected in the microstructure of the CNT forest (Figure 3b), vertical alignment of the CNTs can be observed. This indicates that the additive manufacturing process of the stainless-steel substrates only slightly impacts CNT forest growth. The CNT growth on the manufactured flat plate was then compared with the CNT coating on the Gyroid-TPSf substrate featuring a large ucs of 20 mm and no surrounding cylindrical wall. Both CNT forests exhibit similar overall morphology and height (Figure 3a,c), with barely any differences in their internal structures (Figure 3b,d). This suggests that the substrate surface of the TPMS structure is similarly accessible for CNT growth during CVD synthesis compared to the flat plate. Consequently, it is successfully demonstrated that TPMS structures can serve as effective three-dimensional supports for MWCNT growth, offering a significant increase in the potential catalytic surface area. The uniform growth observed across the entire substrate implies consistent flow through the structure and an even distribution of CNT precursors on its surface. In turn, this suggests that during subsequent catalytic processes, an even distribution of reactants within the reactor can be achieved. The growth, however, changes fundamentally for the subsequent substrates. Lowering the ucs or varying the TPMS type impacts the flow characteristics inside the TPMS substrate and therefore its permeability.[32,35] At an intermediate ucs of 10 mm, the inner surface of the Gyroid-TPnS substrate exhibits an homogeneous CNT coating (Figure 3e), and vertical alignment of the CNT is still observable (Figure 3f). Introducing the external cylindrical wall notably alters the flow behavior throughout the substrate. Open Gyroid-TPnS structures continue to allow for increased mass transfer along the substrate's length compared to closed structures. Encasing


https://doi.org/10.1021/acs.iecr.6c01128
Ind. Eng. Chem. Res. 2026, 65, 16002−16013

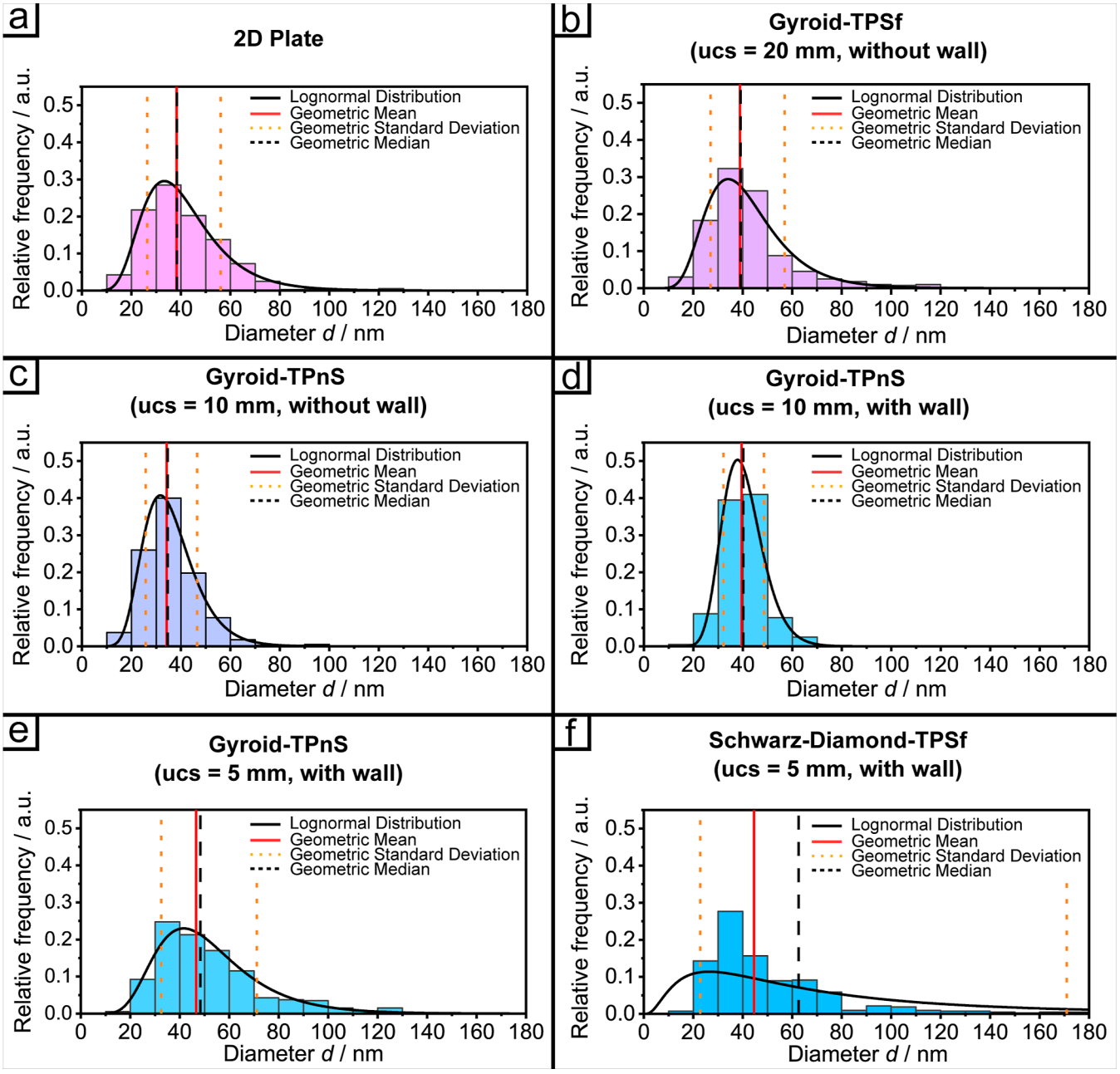


**Figure 4.** Lognormal diameter distribution of CNTs and carbon nanofilaments on different substrates. The geometric mean (red line), the lower and upper limit of the standard deviation (orange dotted lines), and the geometric median (black dashed line) are displayed.

the Gyroid-TPnS structures with the external wall leads to unique flow characteristics.[49] Since no flow can enter or exit from the sides, it is better aligned with the main current. Additionally, the Gyroid-TPnS geometry creates complex flow behavior. Continuous channels thus induce channeling flow, in which the velocities are the highest. There, the dominant direction is along the axial direction. Counter-rotating vortices connect adjacent channels. While flow velocity is the highest in the channels, it is reduced near the substrate surface and struts. This reduces mass and heat transfer perpendicular to the flow while enhancing it along the flow direction.[49] As a consequence, the CNT coating morphology changes fundamentally. A CNT network forms, which spreads horizontally over the inner surface (Figure 3g). The horizontally oriented network not only is located at the center of the Gyroid-TPnS substrate but also extends across its entire inner surface, including the entrance and exit area (Figure S1). Usually, CNT forests grow perpendicular to the surface. For flat surfaces, the spatial limitation induces aligned growth and the formation of CNT forests.[50] We suggest that this laminar-like flow induces high-quality CNT formation via a kite growth mechanism. Due to thermal gradients between the substrate and the gas flow, CNTs are lifted by the gas flow and float above the surface depending on buoyancy and flow velocity. The CNTs align parallel to the surface due to shear forces. This enhances carbon precursor supply to the catalyst, promoting faster growth and ultralong, high-quality CNTs.[51,52] In contrast to classical kite growth, no alignment of the CNTs along a fixed direction can be observed on the Gyroid-TPnS substrate (Figure 3h). Since no distinct flow direction exists near the




https://doi.org/10.1021/acs.iecr.6c01128
Ind. Eng. Chem. Res. 2026, 65, 16002−16013

inner surface, while vortices dominate, CNTs cannot align along a single direction.[49] The result is a CNT network, in which the alignment is parallel to the surface rather than parallel to each other.[49] By decreasing the ucs further to 5 mm, the character of the carbonaceous coating changes. While a horizontal CNT network is still present on the Gyroid-TPnS substrate, islands of spherical carbon structures are observable (Figure 3i). On closer inspection, it becomes apparent that these spherical structures consist of thicker carbon filaments and smaller spherical carbon species (Figure 3j). The development of thick carbon structures instead of a CNT coating suggests a surplus of carbon feedstock in comparison to the amount of active catalytic particles. This could be either due to the increase in the particle size of the catalyst or due to the change of the catalyst-to-carbon-ratio in the interior of the substrate. Similarly to the Gyroid-TPnS structure, the Schwarz-Diamond-TPSf substrate shows a higher affinity of carbon to be deposited on the existing carbon structures than on the actual surface of the substrate. The result is a more pronounced formation of amorphous carbon and suppression of the CNT growth. While some areas of the substrates surface show no carbonaceous growth, the inhomogeneous filamentary carbon structures are still present. The horizontally oriented CNT network found on the previous substrate, however, is absent (Figure 3l). Thick carbon filaments are formed that are made of bundles of thinner filamentary carbon species with diameters of around 50 nm (Figure 3k). Similarly, the interface between residual stainless-steel particles and the substrate surface shows an increased carbonaceous growth. This suggests that the catalyst particles would actually diffuse along the surface of the stainless-steel particle until they get trapped at the interface.[53] These then collide and coalesce, resulting in higher catalyst diameters.[11] The weak growth on the stainless-steel particles can then be attributed to the independent catalytic properties of the stainless-steel material.[54−56]

Since the reaction parameters remained constant for all substrates, the findings indicate that the decreased permeability of the substrate influences the growth conditions greatly. In the work of Acikgöz et al.,[33] it was revealed that as the ucs decreases from 10 mm to 5 mm, the pressure drop across the length of the substrate ($L$ = 40 mm) nearly triples from 109 to 302 Pa. The higher pressure drop is associated with changes in substrate permeability due to more complex internal flow characteristics.[33] In comparison to the Gyroid geometry, the permeability of the Schwarz-Diamond-TPSf structure is decreased further by around 45% at a porosity of 70%.[35] In parallel, the pressure drop along the length of the substrate increases by additional 25 Pa.[33] The graphitic lift off of CNTs will only occur when adhesion strength, the curvature energy, and the interface formation energy between the graphitic cap and the catalyst are balanced out.[57] Thus, the catalyst particle size greatly impacts the growth by showing a less likely CNT growth initiation and an increased encapsulation of the catalyst particle with increasing diameter.[57] We propose that several factors interplay to cause the decline of high-quality CNT networks with decreasing ucs. As ucs decreases, channel diameter shrinks, reducing catalyst particle spacing. Due to lower flow velocities near the surface, catalyst particles are more likely to collide and coalesce.[11,49] As the diffusion of the catalyst is inversely proportional to its size, their mobility is hindered.[11] Since these large particles collect more mobile catalyst particles and carbon precursors, they hinder the homogeneous growth of CNT networks. Moreover, as catalyst particles grow in size, their total number decreases disproportionately due to volume scaling.[11] Beyond a critical catalyst diameter, CNT growth is hindered, and catalyst deactivation occurs.[11] As the carbon precursor is unable to be converted into CNTs, alternative reaction routes lead to the formation of amorphous carbon.[58] Its deposition onto active catalyst particles result in further growth termination.[11,58−60] This interplay of diffusion limitations, catalyst encapsulation, and amorphous carbon promotes the suppression of high-quality CNT formation. A further decrease in permeability results in an increase of amorphous carbon formation and reduces active catalytic sites. The SEM analysis of the coated TPMS substrates reveals that lowering the ucs and adding the external wall induce two distinct morphological changes. The external wall triggers laminar-like flow, promoting kite growth and horizontally oriented, less dense CNT networks. Although this may reduce the total surface area of the CNT, it may improve their accessibility, thereby increasing the catalytically active surface area. When decreasing the ucs below the critical threshold of 10 mm, CNTs transition to other types of carbon species. Generally, this indicates that sufficient permeability of the TPMS structure is crucial. Thus, controlling the flow characteristics inside the substrate can be used to determine the character of the CNT coating. It is unlikely that the morphological differences can be attributed to an increase in reaction temperature inside the substrate as a reduced ucs and the transition to the Schwarz-Diamond-TPSf lead to improved heat transfer.[33]

Figure 4 shows the lognormal diameter distribution of the CNTs and other carbon nanofilaments grown on the six different substrates. Since scanning electron microscopy cannot determine if the internal structure of the carbon structure is of nanotube or nanofiber nature, every filamentary species with a diameter above 80 nm is considered a carbon nanofilament.

The CNT forests grown on the flat substrate and Gyroid-TPnS with a ucs of 20 mm (Figure 4a,b) exhibit similar diameter distributions, with mean diameters of 38 and 39 nm, respectively. When transitioning to the Gyroid-TPnS substrate with a ucs of 10 mm, the diameter distribution narrows steadily. The uniformity of the CNT diameters increases to a maximum as the external wall is added, while the mean diameter remains comparable at 35 and 40 nm (Figure 4c,d). This reinforces the claim that the complex laminar-like flow dynamics in the Gyroid-TPnS leads to the formation of high-quality CNTs as a result of the kite growth mechanism. Below the critical ucs of 10 mm, the diameter distribution broadens significantly (Figure 4e,f). While the Gyroid-TPnS substrate exhibits a CNT network similar to that of the previous structure, thicker carbon nanofilaments are observed (Figure 3j). On the Schwarz-Diamond-TPSf substrate, carbon nanofilaments tend to bundle together and, in some cases, can no longer be distinguished as individual units (Figure 3l). This bundling reduces the overall number of filamentary carbon species as they fuse into bundles with diameters that extend into the micrometer range. The proportion of carbon nanofilaments exceeding 200 nm is approximately 10%, whereas only about 2% exhibit diameters greater than 1000 nm. Although this type of carbon nanostructure is relatively rare, its large size accounts for a majority of the carbon volume present (Figure 3k). Consequently, the diameter distribution is significantly broadened. In Figure S2, the diameter distributions of the Schwarz-Diamond TPSf substrate at a low diameter range and a high diameter range, including the





https://doi.org/10.1021/acs.iecr.6c01128
Ind. Eng. Chem. Res. 2026, 65, 16002−16013

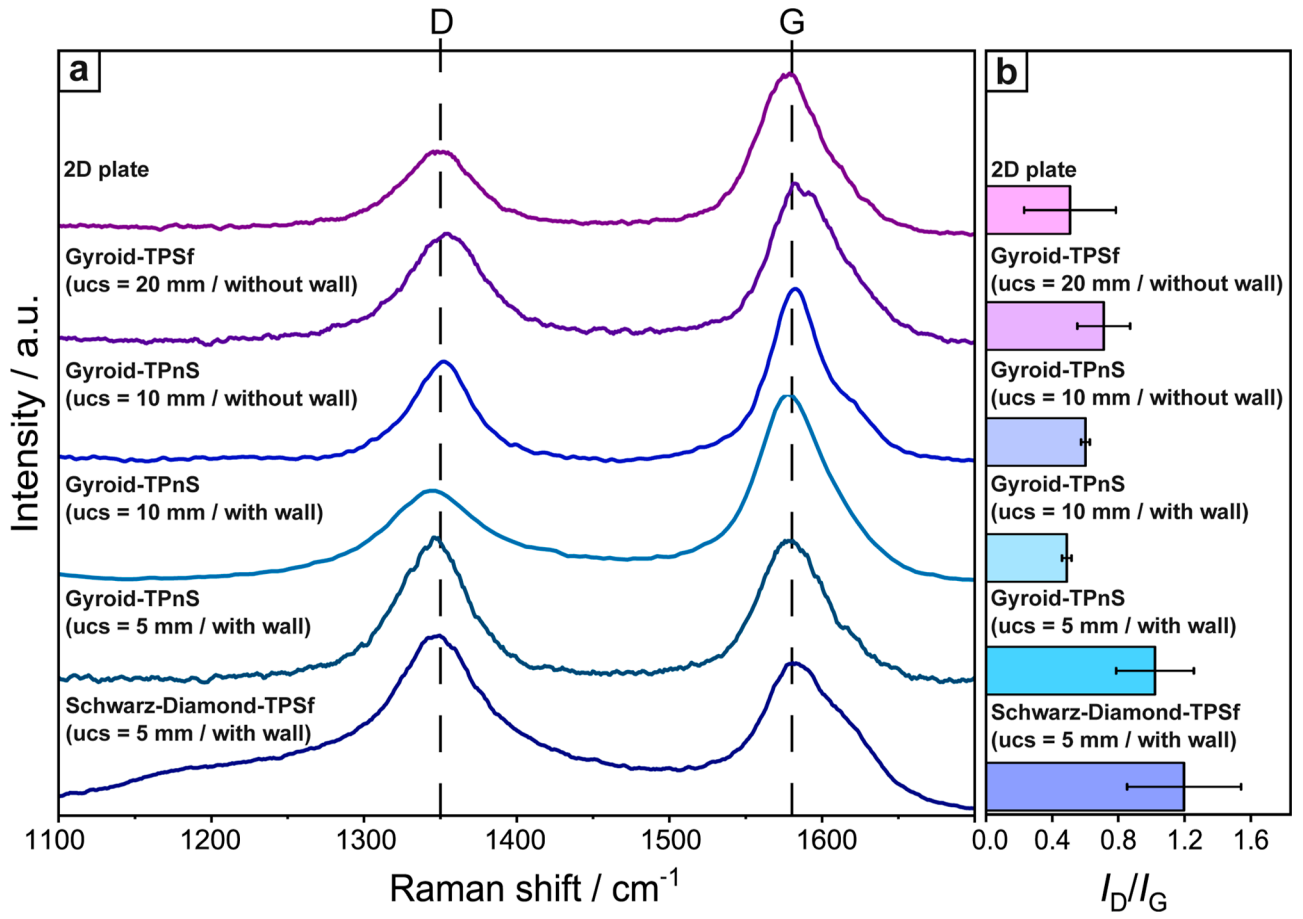


**Figure 5.** Raman spectroscopy of the CNTs grown on the six substrate types. (a) Raman shift indicating the D-band and the G-band and (b) ratio of the D-band intensity $I_D$ and the G-band intensity $I_G$ with its standard deviation. The defect density of the CNT, indicated by the $I_D/I_G$ ratio, increases between the two-dimensional plate and the Schwarz-Diamond-TPSf substrate with decreasing ucs. The Gyroid-TPnS with ucs = 10 mm shows the lowest defect density.

carbon nanofiber bundles, are shown. Due to the increased number and thickness of carbon nanofilaments, the average CNT diameters for substrates with a ucs of 5 mm are elevated. The resulting mean diameters on the Gyroid-TPnS substrate and on the Schwarz-Diamond-TPSf substrate are 48 and 59 nm, respectively. Overall, the diameter distributions indicate that, compared to flat substrates, uniform CNT growth on TPMS structures is possible. A key factor causing diameter inhomogeneity and the formation of diverse carbon nanofilaments is the substrate's permeability. At high ucs, the inner surface of the TPMS remains sufficiently accessible to enable uniform CNT growth. Introducing the external wall results in more uniform diameter distributions due to the laminar-like flow that promotes kite growth. However, below the critical permeability threshold, the diameter distribution widens substantially because of the emergence of thick carbon nanofilaments. Further decreases in permeability promote the formation of a higher proportion of these thicker carbon nanofilaments. While the morphology indicates a clear trend associated with the variation of the TPMS permeability, changes of composition still need to be investigated.

## Impact of Different TPMS-Based Substrates on Defect Density of CNTs

Raman spectroscopy is used to determine the structural quality of the CNT by providing information about the defect density and the degree of graphitization of the CNT. The most relevant peaks for MWCNTs are the D-band at 1350 $cm^{-1}$ and the G-band between 1550 $cm^{-1}$ and 1600 $cm^{-1}$.[61] While the D-band corresponds with the double resonance effect in $sp^2$-carbon and therefore the disorder of the graphitic structure, the G-band is determined by tangential vibrations of graphitic carbon atoms.[61] The Raman spectra for the six different substrate types are shown in Figure 5a. The ratio of the intensities of the Raman bands ($I_D/I_G$) serves as a direct parameter for characterizing the defect density.[62] The corresponding $I_D/I_G$ ratios indicate in good agreement with the previous SEM analysis, a general increase of defect density with decreasing permeability (Figure 5b).

Comparing the $I_D/I_G$ ratio of the additively manufactured flat plate ($I_D/I_G$ = 0.51 ± 0.28) with literature values for MWCNTs grown on silicon[47,63] reveals similar defect densities. Although the ratio increases for the wall-free Gyroid-TPSf (ucs = 20 mm) substrate ($I_D/I_G$ = 0.71 ± 0.16), the defect density remains within the range reported for literature MWCNTs. However, lowering the ucs to 10 mm in the wall-free Gyroid-TPnS substrate reduces the defect density ($I_D/I_G$ = 0.60 ± 0.03.) The CNT network grown on the Gyroid-TPnS (ucs = 10 mm) after introducing the external wall exhibits an even lower defect density ($I_D/I_G$ = 0.48 ± 0.03). This supports that these CNTs result from the kite growth mechanism as ultralong CNTs grown by this process typically exhibit exceptionally low defect densities.[64,65] Since




https://doi.org/10.1021/acs.iecr.6c01128
Ind. Eng. Chem. Res. 2026, 65, 16002−16013

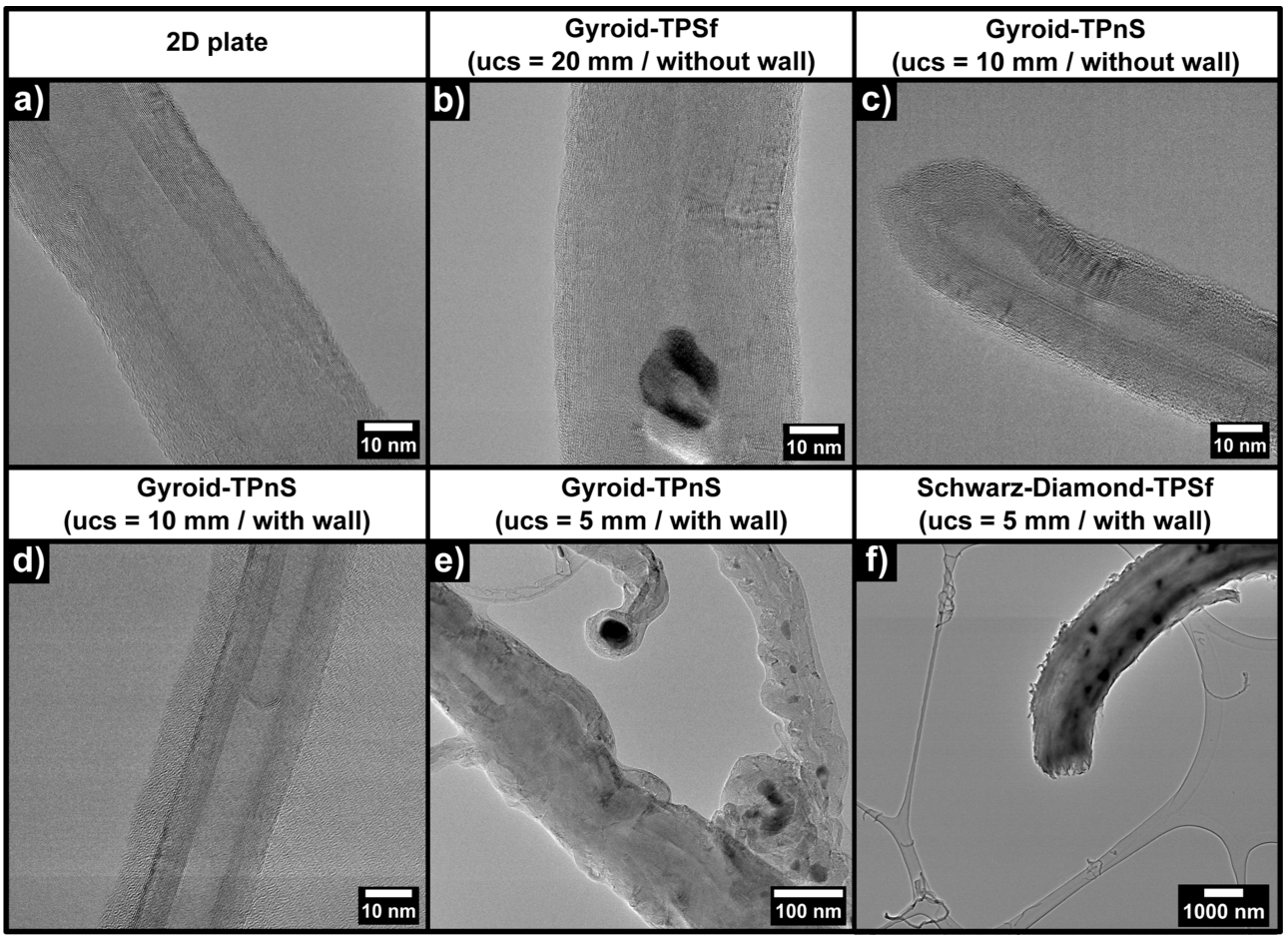


**Figure 6.** Transmission electron microscopy images of carbon nanostructures on the six substrates. For the flat substrate (a) and the Gyroid-TPnS substrates with the ucs of 20 mm (b) and 10 mm (c/d), concentric graphitic layers indicate the growth of carbon nanotubes. Decreasing the ucs further below the critical permeability to 5 mm reveals for the Gyroid-TPnS the formation of carbon nanofibers and their bundling into carbon nanofilaments (e). On the Schwarz-Diamond-TPSf, thick carbon fibers with diameters up to 1000 nm are observed (f).

the CNTs are floating parallel to the surface, the catalyst is highly accessible and therefore enables continuous CNT growth. The wall-free Gyroid-TPnS variant exhibits a transitional state, in which mass transfer along its length is possible due to its open channels. Therefore, the channeling behavior is less developed. A pronounced increase in the $I_D/I_G$ ratio at a ucs of 5 mm to 1.02 ± 0.23 for the Gyroid-TPnS and to 1.20 ± 0.34 for the Schwarz-Diamond-TPSf indicates a significant rise in defect density for substrates below the critical ucs. This suggests the formation of defect-rich carbon species such as amorphous carbon or carbon nanofibers (CNFs). Additionally, the Raman spectrum of the Schwarz-Diamond-TPSf substrate exhibits broadened and partially merged D- and G-bands. A further saddle point is observed at a Raman shift of approximately 1200 $cm^{-1}$. These spectral features correspond to additional sub-D bands and indicate the presence of substantial amounts of amorphous carbon.[66] Furthermore, the standard deviation of the $I_D/I_G$ ratios is high across most substrate types, indicating generally inhomogeneous CNT growth on the additively manufactured structures. This inhomogeneity can be attributed to the surface roughness and wavy morphology caused by the fused spherical stainless-steel particles. Variations in surface morphology affect the catalyst particle size distribution and, consequently, the quality of the CNT.[53] An exception is observed on the Gyroid-TPnS substrates with the ucs of 10 mm, on which the standard deviation is notably low. We propose that this more homogeneous CNT growth results from the high growth rates to the kite growth mechanism caused by the three-dimensional laminar-like state flow through the substrate.[49] Because growth termination is less probable, the length of the highly graphitic CNT is increased. Consequently, the proportion of these high-quality CNTs within the overall carbon content is raised.

The Raman spectra consistently confirm successful CNT growth on both additively manufactured stainless-steel and TPMS-based substrates. A correlation between the substrate permeability and defect density is evident. Above a critical ucs, the defect density remained comparatively low. The emergence of kite growth due to laminar-like flow and sufficient permeability reduces the defect density to a minimum; however, once the permeability threshold is exceeded, the defect density increases sharply. Reduced permeability within the TPMS structure likely limits efficient carbon precursor transport, preventing complete conversion to graphitic layers and thereby promoting the formation of amorphous carbon.

## Structure of Different Carbon Nanofilaments on TPMS-Based Substrates

To investigate the origin of the various carbon nanospecies on the six substrates, transmission electron microscopy images were obtained (Figure 6). The catalyst nanoparticles are





https://doi.org/10.1021/acs.iecr.6c01128
Ind. Eng. Chem. Res. 2026, 65, 16002−16013

depicted as dark dots with low transparency, whereas the carbonaceous materials are more transparent. Graphitic areas can be recognized by concentric lattice planes aligned parallel to the surface. If the lattice planes are diffuse, the carbon is amorphous. It should be noted that amorphous carbon often exhibits small graphitic areas due to the crystallization of the carbon by the electron beam.[66] Therefore, the appearance of these areas does not generally exclude the presence of amorphous carbon.

Transmission electron microscopy (TEM) images of the CNTs grown on the flat plate (Figure 6a) and the Gyroid-TPSf substrates with the ucs of 20 mm (Figure 6b) and 10 mm with and without the cylindrical wall (Figure 6c,d) confirm the successful synthesis of CNTs. Features such as concentrically oriented graphitic layers and hollow cores provide strong evidence of successful CNT growth on TPMS substrates. Upon further reduction of the ucs to 5 mm, a critical threshold is reached. The growth behavior on the Gyroid-TPnS (Figure 6e) and Schwarz-Diamond-TPSf (Figure 6f) substrates changes significantly in terms of their morphology and structure. Below this critical ucs, primarily carbon nanofibers (CNFs) are formed. CNFs are characterized by their relatively large diameters, ranging from 50 to 200 nm, rough surface textures, and complex internal structures. Their morphology is identifiable by misaligned and discontinuous graphitic layers, as well as irregular tubular voids.[67] While isolated CNFs can be observed, they predominantly appear as bundles. Amorphous carbon is visible on their surfaces, acting as a linking interphase. On the Schwarz-Diamond-TPSf substrate, thick carbon filaments with diameters exceeding 1000 nm can be observed, as depicted in Figure 6f. However, their precise structural compositions remain unclear. Because of their large diameters, lattice planes are not identifiable. Higher-contrast regions within these filaments indicate the presence of catalyst particles of varying sizes. Randomly oriented CNFs and disordered carbon layers are observed at the filament edges. Therefore, we propose that these thick carbon filaments primarily consist of bundled CNFs agglomerated through large amounts of amorphous carbon. This observation emphasizes that as the substrate permeability decreases below the critical threshold, the proportion of amorphous carbon increases. Amorphous carbon coats catalyst particles, preventing the lift-off of CNT caps, which results in catalyst encapsulation and inhibited growth.[68] Nevertheless, due to the high synthesis temperature, CNT nucleation can still occur prior to termination, while hydrogen etching removes the amorphous coating and enables constant catalyst reactivation.[68] Overall, this leads to a complex growth process, where carbonaceous coating and catalyst reactivation result in the formation of large carbon nanofilaments. On the basis of these findings, we propose that a minimal permeability is required for the homogeneous growth of MWCNTs. Above the critical ucs, the CNT grows successfully on TPMS substrates. Once the threshold is crossed, CNF growth is induced due to excessive deposition of amorphous carbon. When permeability is further reduced, thick carbon nanofilaments with diameters exceeding 1000 nm form due to the agglomeration of the CNF.

## CONCLUSION

This work investigates the impact of the permeability of TPMS-based substrates on the growth of CNT forests. PBF-LB/M was utilized to tailor the ucs and type of the substrates, thereby enabling a controlled tuning of its permeability. Three core observations can be made.

1 The growth of CNT coatings on TPMS structures is possible up to a critical permeability.
2 The introduction of an external wall induces the kite growth mechanism and the formation of horizontally oriented high-quality CNT networks due to the channeling flow behavior.
3 Below this critical value, the proportion of the amorphous carbon increases. As it settles on the surface of the substrate and the CNT, it partially terminates the growth of the CNT and leads to the formation of defect-rich carbon nanofilaments.

Overall, this work demonstrates the viability of CNT coatings on complex three-dimensional TPMS structures, effectively combining the high catalytic surface area of the CNT coating with the superior flow dynamics and heat- and mass-transfer properties of TPMS geometries. Tailoring of the CNT morphology was achieved by modifying the substrate. This smart reactor design thus represents a direct competitor to the fixed-bed reactor, which features a high active surface area and complex flow dynamics. Nonetheless, challenges related to the complex growth behavior of CNTs on TPMS substrates with low unit cell sizes remain to be addressed. The successful integration of CNTs into the smart reactor design of TPMS structures, leveraging their exceptional thermal and electrical conductivity, as well as their unique wetting behavior, unlocks numerous new possibilities for adaptive and responsive reactor operations.

## ASSOCIATED CONTENT

### Data Availability Statement

The SEM and TEM microscopy images obtained by Zeiss Supra 55 VP and FEI Talos F200X and the Raman spectra of the CNT obtained by the TriVista 557 system are openly available in TORE at 10.15480/882.16831.

### Supporting Information

The Supporting Information is available free of charge at https://pubs.acs.org/doi/10.1021/acs.iecr.6c01128.

SEM images of Gyroid-TPnS (ucs = 10 mm, no wall) on four different substrate positions (Figure S1), diameter distribution of Schwarz-Diamond-TPSf at low and high diameter ranges (Figure S2), SEM images of the coating on the six substrates (Figure S3), and diameter distribution and defect density values of various substrates (Table S1) (PDF)

## AUTHOR INFORMATION


### Corresponding Author

**Fabian Riebesehl** − *Institute of Polymers and Composites, Hamburg University of Technology, Hamburg 21073, Germany*; orcid.org/0009-0003-2611-7688; Email: fabian.riebesehl@tuhh.de

### Authors

**Serhan Acikgöz** − *Institute for Industrialization of Smart Materials, Hamburg University of Technology, Hamburg 21079, Germany*

**Timo Merbach** − *Institute of Multiphase Flows, Hamburg University of Technology, Hamburg 21073, Germany*

**Christiane Roller** − *Institute of Polymers and Composites, Hamburg University of Technology, Hamburg 21073, Germany;* orcid.org/0009-0006-3350-3378
**Dominique Lumpp** − *Institute of Technical and Macromolecular Chemistry, University of Hamburg, Hamburg 20146, Germany;* orcid.org/0009-0008-4083-0355
**Dirk Herzog** − *Institute for Industrialization of Smart Materials, Hamburg University of Technology, Hamburg 21079, Germany; Fraunhofer Research Institution for Additive Production Technologies, Hamburg 21029, Germany*
**Jakob Albert** − *Institute of Technical and Macromolecular Chemistry, University of Hamburg, Hamburg 20146, Germany;* orcid.org/0000-0002-3923-2269
**Ingomar Kelbassa** − *Fraunhofer Research Institution for Additive Production Technologies, Hamburg 21029, Germany*
**Michael Schlüter** − *Institute of Multiphase Flows, Hamburg University of Technology, Hamburg 21073, Germany*
**Bodo Fiedler** − *Institute of Polymers and Composites, Hamburg University of Technology, Hamburg 21073, Germany;* orcid.org/0000-0002-2734-1353

Complete contact information is available at: https://pubs.acs.org/10.1021/acs.iecr.6c01128

## Author Contributions

**Conceptualization:** Fabian Riebesehl, Serhan Acikgöz, Timo Merbach, Dirk Herzog, Jakob Albert, Ingomar Kelbassa, Michael Schlüter, Bodo Fiedler. **Experimental setup and measurements:** Fabian Riebesehl, Serhan Acikgöz, Christiane Roller. **Formal analysis and data curation:** Fabian Riebesehl, Serhan Acikgöz. **Writing—original draft:** Fabian Riebesehl, Serhan Acikgöz. **Writing—review and editing:** Fabian Riebesehl, Serhan Acikgöz, Christiane Roller, Dominique Lumpp, Timo Merbach. **Funding acquisition:** Bodo Fiedler, Michael Schlüter, Ingomar Kelbassa, Jakob Albert. All authors have read and agreed to the published version of the manuscript.

## Notes

The authors declare no competing financial interest.

## ■ ACKNOWLEDGMENTS

This project was funded by the Deutsche Forschungsgemeinschaft (DFG, German Research Foundation), SFB 1615−503850735. We thank DFG for the funding. The authors thank Aaron D. Pfleger for the kind assistance with Raman spectroscopy and Olaf Wittleben for the preparation of the different slices of the TPMS substrates and the Electron Microscopy Unit (BeEM) at the Hamburg University of Technology (TUHH) for providing access to the scanning electron microscope and transmission electron microscope.

## ■ REFERENCES

(1) Moyer-Vanderburgh, K.; Park, S. J.; Fornasiero, F. Growth of carbon nanotube forests on flexible metal substrates: Advances, challenges, and applications. *Carbon* **2023**, *206*, 402−421.
(2) Wang, P.; Dong, Q.; Gao, C.; Bai, W.; Chu, D.; He, Y. A comprehensive review of carbon nanotubes: growth mechanisms, preparation and applications. *Fullerenes, Nanotub. Carbon Nanostruct.* **2024**, *32*, 415−429.
(3) Ping, L.; Hou, P.-X.; Liu, C.; Cheng, H.-M. Vertically aligned carbon nanotube arrays as a thermal interface material. *APL Mater.* **2019**, *7*, 020902.
(4) Huang, S.; Du, X.; Ma, M.; Xiong, L. Recent progress in the synthesis and applications of vertically aligned carbon nanotube materials. *Nanotechnol. Rev.* **2021**, *10*, 1592−1623.
(5) Wang, Z.; Ci, L.; Chen, L.; Nayak, S.; Ajayan, P. M.; Koratkar, N. Polarity-Dependent Electrochemically Controlled Transport of Water through Carbon Nanotube Membranes. *Nano Lett.* **2007**, *7*, 697−702.
(6) Andrews, R.; Jacques, D.; Rao, A.; Derbyshire, F.; Qian, D.; Fan, X.; Dickey, E.; Chen, J. Continuous production of aligned carbon nanotubes: a step closer to commercial realization. *Chem. Phys. Lett.* **1999**, *303*, 467−474.
(7) Sinnott, S.; Andrews, R.; Qian, D.; Rao, A.; Mao, Z.; Dickey, E.; Derbyshire, F. Model of carbon nanotube growth through chemical vapor deposition. *Chem. Phys. Lett.* **1999**, *315*, 25−30.
(8) Guzmán De Villoria, R.; Hart, A. J.; Wardle, B. L. Continuous High-Yield Production of Vertically Aligned Carbon Nanotubes on 2D and 3D Substrates. *ACS Nano* **2011**, *5*, 4850−4857.
(9) Orbaek, A. W.; Aggarwal, N.; Barron, A. R. The development of a 'process map' for the growth of carbon nanomaterials from ferrocene by injection CVD. *J. Mater. Chem. A* **2013**, *1*, 14122.
(10) Shah, K. A.; Tali, B. A. Synthesis of carbon nanotubes by catalytic chemical vapour deposition: A review on carbon sources, catalysts and substrates. *Mater. Sci. Semicond. Process.* **2016**, *41*, 67−82.
(11) Gakis, G.; Chrysoloras, T.; Aviziotis, I.; Charitidis, C. Towards a mechanistic understanding of the floating catalyst CVD of CNTs: Interplay between catalyst particle nucleation, growth and deactivation. *Chem. Eng. Sci.* **2024**, *295*, 120204.
(12) Bedewy, M. Data-driven understanding of collective carbon nanotube growth by *in situ* characterization and nanoscale metrology. *J. Mater. Res.* **2017**, *32*, 153−165.
(13) Xu, T.; Wang, Z.; Miao, J.; Chen, X.; Tan, C. M. Aligned carbon nanotubes for through-wafer interconnects. *Appl. Phys. Lett.* **2007**, *91*, 042108.
(14) Mutha, H. K.; Lu, Y.; Stein, I. Y.; Cho, H. J.; Suss, M. E.; Laoui, T.; Thompson, C. V.; Wardle, B. L.; Wang, E. N. Porosimetry and packing morphology of vertically aligned carbon nanotube arrays via impedance spectroscopy. *Nanotechnology* **2017**, *28*, 05LT01.
(15) Lumpp, D.; Shaikh, S.; Riebesehl, F.; Ruhmlieb, C.; Kruber, K.; Schroeter, B.; Smirnova, I.; Skiborowski, M.; Fiedler, B.; Albert, J. Multifunctional Carbon-Nanotube Supported Catalyst for Efficient Glycerol Hydrogenolysis to 1,2-propanediol. *ChemCatChem* **2026**, *18*, No. e01748.
(16) Sherbi, M.; Wesner, A.; Wisniewski, V. K.; Bukowski, A.; Velichkova, H.; Fiedler, B.; Albert, J. Superior CNT-supported bimetallic RuCu catalyst for the highly selective hydrogenolysis of glycerol to 1,2-propanediol. *Catal. Sci. Technol.* **2021**, *11*, 6649−6653.
(17) Serp, P.; Castillejos, E. Catalysis in Carbon Nanotubes. *ChemCatChem* **2010**, *2*, 41−47.
(18) Rodríguez-reinoso, F. The role of carbon materials in heterogeneous catalysis. *Carbon* **1998**, *36*, 159−175.
(19) Handuja, S.; Srivastava, P.; Vankar, V. D. On the Growth and Microstructure of Carbon Nanotubes Grown by Thermal Chemical Vapor Deposition. *Nanoscale Res. Lett.* **2010**, *5*, 1211−1216.
(20) Fan, W.; Wang, Y.; Chen, J.; Yuan, Y.; Li, A.; Wang, Q.; Wang, C. Controllable growth of uniform carbon nanotubes/carbon nanofibers on the surface of carbon fibers. *RSC Adv.* **2015**, *5*, 75735−75745.
(21) Förster, T.; Hao, B.; Mäder, E.; Simon, F.; Wölfel, E.; Ma, P.-C. CVD-Grown CNTs on Basalt Fiber Surfaces for Multifunctional Composite Interphases. *Fibers* **2016**, *4*, 28.
(22) Yamamoto, N.; John Hart, A.; Garcia, E. J.; Wicks, S. S.; Duong, H. M.; Slocum, A. H.; Wardle, B. L. High-yield growth and morphology control of aligned carbon nanotubes on ceramic fibers for multifunctional enhancement of structural composites. *Carbon* **2009**, *47*, 551−560.

(23) Miao, J. Y.; Cai, Y.; Chan, Y. F.; Sheng, P.; Wang, N. A Novel Carbon Nanotube Structure Formed in Ultra-Long Nanochannels of Anodic Aluminum Oxide Templates. *J. Phys. Chem. B* **2006**, *110*, 2080−2083.
(24) Pérez-Cadenas, M.; Muñoz-Andrés, V.; Rodríguez-Ramos, I.; Maroto-Valiente, A.; Guerrero-Ruíz, A. Building up Multiwall Carbon Nanotubes Nanostructures inside Millimetric Channels of Ceramic Monoliths. *J. Nano Res.* **2012**, *18*−*19*, 271−279.
(25) Worsley, M. A.; Stadermann, M.; Wang, Y. M.; Satcher Jr, J. H.; Baumann, T. F. High surface area carbon aerogels as porous substrates for direct growth of carbon nanotubes. *Chem. Commun.* **2010**, *46*, 9253.
(26) Suryavanshi, U.; Baskar, A. V.; Balasubramanian, V. V.; Al-Deyab, S. S.; Al-Enizi, A.; Vinu, A. Growth and physico-chemical properties of interconnected carbon nanotubes in FeSBA-15 mesoporous molecular sieves. *Arabian J. Chem.* **2016**, *9*, 171−178.
(27) Al-Ketan, O.; Rowshan, R.; Abu Al-Rub, R. K. Topology-mechanical property relationship of 3D printed strut, skeletal, and sheet based periodic metallic cellular materials. *Addit. Manuf.* **2018**, *19*, 167−183.
(28) Qu, S.; Ding, J.; Song, X. Achieving Triply Periodic Minimal Surface Thin-Walled Structures by Micro Laser Powder Bed Fusion Process. *Micromachines* **2021**, *12*, 705.
(29) Tang, W.; Zhou, H.; Zeng, Y.; Yan, M.; Jiang, C.; Yang, P.; Li, Q.; Li, Z.; Fu, J.; Huang, Y.; Zhao, Y. Analysis on the convective heat transfer process and performance evaluation of Triply Periodic Minimal Surface (TPMS) based on Diamond, Gyroid and Iwp. *Int. J. Heat Mass Transfer* **2023**, *201*, 123642.
(30) Kladovasilakis, N.; Tsongas, K.; Kostavelis, I.; Tzovaras, D.; Tzetzis, D. Effective mechanical properties of additive manufactured triply periodic minimal surfaces: experimental and finite element study. *Int. J. Adv. Des. Manuf. Technol.* **2022**, *121*, 7169−7189.
(31) Reynolds, B. W.; Fee, C. J.; Morison, K. R.; Holland, D. J. Characterisation of Heat Transfer within 3D Printed TPMS Heat Exchangers. *Int. J. Heat Mass Transfer* **2023**, *212*, 124264.
(32) Asbai-Ghoudan, R.; Ruiz De Galarreta, S.; Rodriguez-Florez, N. Analytical model for the prediction of permeability of triply periodic minimal surfaces. *J. Mech. Behav. Biomed. Mater.* **2021**, *124*, 104804.
(33) Acikgöz, S.; Wigger, C.; Merbach, T.; Kexel, F.; Maiwald, M. I.; Herzog, D.; Kelbassa, I.; Schlüter, M. Design guidelines for laser powder bed fusion of triply periodic minimal surface structures for applications in smart reactors. *Progr. Addit. Manuf.* **2026**, *11*, 2215.
(34) Karcher, H.; Polthier, K. Construction of triply periodic minimal aces. *Philos. Trans. A. Math. Phys. Eng. Sci.* **1996**, *354*, 2077−2104.
(35) Santos, J.; Pires, T.; Gouveia, B. P.; Castro, A. P.; Fernandes, P. R. On the permeability of TPMS scaffolds. *J. Mech. Behav. Biomed. Mater.* **2020**, *110*, 103932.
(36) Naghavi, S. A.; Tamaddon, M.; Marghoub, A.; Wang, K.; Babamiri, B. B.; Hazeli, K.; Xu, W.; Lu, X.; Sun, C.; Wang, L.; Moazen, M.; Wang, L.; Li, D.; Liu, C. Mechanical Characterisation and Numerical Modelling of TPMS-Based Gyroid and Diamond Ti6Al4V Scaffolds for Bone Implants: An Integrated Approach for Translational Consideration. *Bioengineering* **2022**, *9*, 504.
(37) Bakhtari, A. R.; Sezer, H. K.; Canyurt, O. E.; Eren, O.; Shah, M.; Marimuthu, S. A Review on Laser Beam Shaping Application in Laser-Powder Bed Fusion. *Adv. Eng. Mater.* **2024**, *26*, 2302013.
(38) Fisher, J. W.; Miller, S. W.; Bartolai, J.; Simpson, T. W.; Yukish, M. A. Catalog of triply periodic minimal surfaces, equation-based lattice structures, and their homogenized property data. *Data Brief* **2023**, *49*, 109311.
(39) Stiegler, T.; Meltzer, K.; Tremel, A.; Baldauf, M.; Wasserscheid, P.; Albert, J. Development of a Structured Reactor System for $CO_2$ Methanation under Dynamic Operating Conditions. *Energy Technol.* **2019**, *7*, 1900047.
(40) Wolf, T.; Fu, Z.; Ye, J.; Heßelmann, C.; Pistor, J.; Albert, J.; Wasserscheid, P.; Körner, C. Periodic Open Cellular Raney-Copper Catalysts Fabricated via Selective Electron Beam Melting. *Adv. Eng. Mater.* **2020**, *22*, 1901524.
(41) Heßelmann, C.; Wolf, T.; Galgon, F.; Körner, C.; Albert, J.; Wasserscheid, P. Additively manufactured RANEY®-type copper catalyst for methanol synthesis. *Catal. Sci. Technol.* **2020**, *10*, 164−168.
(42) Horn, R. In *Handbook of Chemical Reactors*, Reschetilowski, W., Ed.; Springer Berlin Heidelberg: Berlin, Heidelberg, 2026; pp 559−623.
(43) Ountaksinkul, K.; Sripinun, S.; Bumphenkiattikul, P.; Vongachariya, A.; Praserthdam, P.; Assabumrungrat, S. A Review of Packed Bed Reactor and Gradient-less Recycle Reactor for Determination of Intrinsic Reaction Kinetics. *Eng. J.* **2022**, *26*, 17−42.
(44) Yildiz, O.; Lubna, M. M.; Ramesh, V. P.; Ozturk, M.; Bradford, P. D. Microporous vertically aligned CNT nanocomposites with tunable properties for use in flexible heat sinks. *J. Sci.:Adv. Mater. Devices* **2022**, *7*, 100509.
(45) Park, S. J.; Ok, J. G.; Park, H. J.; Lee, K.-T.; Lee, J. H.; Kim, J. D.; Cho, E.; Baac, H. W.; Kang, S.; Guo, L. J.; Hart, A. J. Modulation of the effective density and refractive index of carbon nanotube forests via nanoimprint lithography. *Carbon* **2018**, *129*, 8−14.
(46) Fratalocchi, L.; Groppi, G.; Visconti, C. G.; Lietti, L.; Tronconi, E. Packed-POCS with skin: A novel concept for the intensification of non-adiabatic catalytic processes demonstrated in the case of the Fischer−Tropsch synthesis. *Catal. Today* **2022**, *383*, 15−20.
(47) Kröning, K.; Krause, B.; Pötschke, P.; Fiedler, B. Nanocomposites with p- and n-Type Conductivity Controlled by Type and Content of Nanotubes in Thermosets for Thermoelectric Applications. *Nanomaterials* **2020**, *10*, 1144.
(48) Schneider, C. A.; Rasband, W. S.; Eliceiri, K. W. NIH Image to ImageJ: 25 years of image analysis. *Nat. Methods* **2012**, *9*, 671−675.
(49) Merbach, T.; Adrian, M.; Wigger, C.; Iraqi Houssaini, S.; Bayer, B.; Tsanda, A.; Acikgöz, S.; Weiland, C.; Kexel, F.; Herzog, D.; Hoffmann, M.; Kelbassa, I.; Knopp, T.; Penn, A.; Schlüter, M. Comprehensive study of 3D liquid flow fields in additive manufactured structures for SMART reactors using large-scale vertical magnetic resonance imaging and computational fluid dynamics. *Chem. Eng. J.* **2026**, *539*, 176536.
(50) Wei, B. Q.; Vajtai, R.; Jung, Y.; Ward, J.; Zhang, R.; Ramanath, G.; Ajayan, P. M. Organized assembly of carbon nanotubes. *Nature* **2002**, *416*, 495−496.
(51) Jiang, Q.; Wang, F.; Li, R.; Wu, X.; Zhang, W.; Zhao, S.; Huang, Y.; Wang, B.; Zhang, S.; Zhao, Y.; Zhang, R. The Inherent Thermal Effect of Substrates on the Growth of Ultralong Carbon Nanotubes. *Adv. Funct. Mater.* **2023**, *33*, 2212665.
(52) Jin, Z.; Chu, H.; Wang, J.; Hong, J.; Tan, W.; Li, Y. Ultralow Feeding Gas Flow Guiding Growth of Large-Scale Horizontally Aligned Single-Walled Carbon Nanotube Arrays. *Nano Lett.* **2007**, *7*, 2073−2079.
(53) Lee, G.; Kim, K. J.; Yu, W. R.; Youk, J. H. The effect of the surface roughness of carbon fibres on CNT growth by floating-catalyst chemical vapour deposition. *Int. J. Nanotechnol.* **2013**, *10*, 800.
(54) Baddour, C. E.; Fadlallah, F.; Nasuhoglu, D.; Mitra, R.; Vandsburger, L.; Meunier, J.-L. A simple thermal CVD method for carbon nanotube synthesis on stainless steel 304 without the addition of an external catalyst. *Carbon* **2009**, *47*, 313−318.
(55) Pakdee, U.; Chiangga, S.; Suwannatus, S.; Limsuwan, P. Growth of MWCNTs on Flexible Stainless Steels without Additional Catalysts. *J. Nanomater.* **2017**, *2017*, 1−11.
(56) Hordy, N.; Mendoza-Gonzalez, N.-Y.; Coulombe, S.; Meunier, J.-L. The effect of carbon input on the morphology and attachment of carbon nanotubes grown directly from stainless steel. *Carbon* **2013**, *63*, 348−357.
(57) Ding, L. P.; McLean, B.; Xu, Z.; Kong, X.; Hedman, D.; Qiu, L.; Page, A. J.; Ding, F. Why Carbon Nanotubes Grow. *J. Am. Chem. Soc.* **2022**, *144*, 5606−5613.
(58) Nessim, G. D. Properties, synthesis, and growth mechanisms of carbon nanotubes with special focus on thermal chemical vapor deposition. *Nanoscale* **2010**, *2*, 1306.

(59) Pattinson, S. W.; Prehn, K.; Kinloch, I. A.; Eder, D.; Koziol, K. K. K.; Schulte, K.; Windle, A. H. The life and death of carbon nanotubes. *RSC Adv.* **2012**, *2*, 2909.
(60) Stadermann, M.; Sherlock, S. P.; In, J.-B.; Fornasiero, F.; Park, H. G.; Artyukhin, A. B.; Wang, Y.; De Yoreo, J. J.; Grigoropoulos, C. P.; Bakajin, O.; Chernov, A. A.; Noy, A. Mechanism and Kinetics of Growth Termination in Controlled Chemical Vapor Deposition Growth of Multiwall Carbon Nanotube Arrays. *Nano Lett.* **2009**, *9*, 738−744.
(61) Lehman, J. H.; Terrones, M.; Mansfield, E.; Hurst, K. E.; Meunier, V. Evaluating the characteristics of multiwall carbon nanotubes. *Carbon* **2011**, *49*, 2581−2602.
(62) Li, Z.; Deng, L.; Kinloch, I. A.; Young, R. J. Raman spectroscopy of carbon materials and their composites: Graphene, nanotubes and fibres. *Prog. Mater. Sci.* **2023**, *135*, 101089.
(63) Plunkett, A.; Kröning, K.; Fiedler, B. Highly Optimized Nitrogen-Doped MWCNTs through In-Depth Parametric Study Using Design of Experiments. *Nanomaterials* **2019**, *9*, 643.
(64) Zhang, R.; Zhang, Y.; Zhang, Q.; Xie, H.; Qian, W.; Wei, F. Growth of Half-Meter Long Carbon Nanotubes Based on Schulz−Flory Distribution. *ACS Nano* **2013**, *7*, 6156−6161.
(65) Tsuji, T.; Hata, K.; Futaba, D. N.; Sakurai, S. Additional obstacles in carbon nanotube growth by gas-flow directed chemical vapour deposition unveiled through improving growth density. *Nanoscale Adv.* **2019**, *1*, 4076−4081.
(66) Moseenkov, S. I.; Kuznetsov, V. L.; Zolotarev, N. A.; Kolesov, B. A.; Prosvirin, I. P.; Ishchenko, A. V.; Zavorin, A. V. Investigation of Amorphous Carbon in Nanostructured Carbon Materials (A Comparative Study by TEM, XPS, Raman Spectroscopy and XRD). *Materials* **2023**, *16*, 1112.
(67) Meftahi, A.; Kashef Sabery, M. S.; Alibakhshi, S.; Walsh, M.; Bechelany, M.; Naseef, A.; Barhoum, A. Carbon nanotubes and nanofibers as building blocks for the future: Structure, synthesis, properties, and functionalization perspectives. *Mater. Sci. Eng. B* **2025**, *322*, 118622.
(68) Schünemann, C.; Schäffel, F.; Bachmatiuk, A.; Queitsch, U.; Sparing, M.; Rellinghaus, B.; Lafdi, K.; Schultz, L.; Büchner, B.; Rümmeli, M. H. Catalyst Poisoning by Amorphous Carbon during Carbon Nanotube Growth: Fact or Fiction? *ACS Nano* **2011**, *5*, 8928−8934.





https://doi.org/10.1021/acs.iecr.6c01128
*Ind. Eng. Chem. Res.* 2026, 65, 16002−16013